Experimental Analysis of Hydrodynamics in Axially Agitated Tank

Stephan Bugay, Renaud Escudié, and Alain Liné
Laboratoire d'Ingénierie des Procédés de l'Environnement, Institut National des Sciences Appliquées de Toulouse, 31077 Toulouse Cedex, France

Particle image velocimetry (PIV) technique was used to analyze the flow field in a stirred tank induced by a Lightnin A310 axial impeller, focusing on the hydrodynamics, with particular attention to turbulence [production, transport, and dissipation rate of turbulent kinetic energy (TKE)]. The first data of interest are the three components of the mean velocity, which give the overall circulation in the tank. Since turbulence controls mainly the mixing, the six components of the Reynolds stresses were measured. The dissipation rate of TKE was estimated after an experimental evaluation of the different terms of the TKE balance equation at different levels in the tank. A profile close to the impeller is compared to previous empirical modeling where the dissipation rate of TKE was related to the level of TKE and to a macroscale of turbulence that was assumed to be proportional to the impeller.

Introduction

Mechanically agitated tanks are widely used in chemical engineering. Empirical rules have been developed in the past to design impellers and vessels. In recent years, the increasing efficiency of both experimental tools [such as particle image velocimetry (PIV)] and numerical codes [computational fluid dynamics (CFD)] enables a local analysis of the flow field in a vessel to be developed in order to improve mixing. Local experiments constitute data banks that permit a better understanding of the local phenomena; such data banks are used in testing the validity of CFD simulations. In particular, it is possible to determine the level of turbulence modeling that is necessary and sufficient to reproduce the main physical trends in an agitated tank (Naude et al., 1998; Derksen and van den Akker, 1999; Essemiani, 2000).

The present article focuses on the application of the PIV technique to analyze locally the hydrodynamics structure in an axially agitated tank. Although the study concentrates on the region just below the impeller, experimental data within the whole tank is described (Bugay, 1998; Escudié, 1998). The study is restricted to one axial flow impeller (Lightnin A310).

A good understanding of the phenomena controlling impeller discharge is needed. At a large Reynolds number, the axial flow is induced by the impeller; an efficient lift is exerted by the blades of the impeller on the liquid. The lift is induced by pressure distribution above and below the blades. The vertical pressure difference creates a vertical or axial flow. The choice of the Lightnin A310 impeller is related to this hydrofoil characteristic. In addition, the shape of the impeller induces a weak tangential form drag.

Basically, the flow field induced by any impeller is not steady (see Myers et al., 1997). The motion of the blades of any impeller can induce periodic fluctuations. This is the case for a Rushton turbine. It is well known that phase averaging is essential in the case of a Rushton turbine, in order to separate the random turbulence and periodic component induced by the trailing vortices generated by such simple blades (see van't Riet et al., 1976; van der Molen and van Maanen, 1978; Mahouast et al., 1989; Wu and Patterson, 1993; Escudié et al., 2000). Such trailing vortices have been analyzed in detail in the case of the Rushton turbine or pitch-blade turbine (van't Riet and Smith, 1975; Lee and Yanneskis, 1998; Derksen et al., 1999).

In fact, phase averaging is not essential in the case of shaped impellers, such as an axial impeller (Weetman and Oldshue, 1988; Escudié et al., 2002). Indeed, the A310 impeller design has been based on airfoil techniques (Abbot and Von Doenhoff, 1959) and no significant trailing vortices are generated (Zhou and Kresta, 1996b; Ducoste et al., 1997).

Correspondence concerning this article should be addressed to A. Liné.

Thus, the motion of the blades of the impeller induces negligible periodic fluctuations, so statistical analyses developed in this article have been performed without phase averaging with respect to the position of the impeller.

Many years ago, Cutter (1966) used a photographic technique to develop a pioneering approach to determine the velocity field. The displacement measurement of seeding particles was carried out by hand, so the number of events was limited. More recently, Myers et al. (1997) and Bakker et al. (1996) applied the PIV technique to analyze macroinstabilities in agitated tanks. Perrard et al. (2000) and Escudié et al. (2000) applied the PIV technique to study mixing in an agitated tank with a Rushton turbine.

In fact, very few studies have been devoted to axial-flow impellers, such as the Lightnin A310. Mavros et al. (1996) and Chapple and Kresta (1994) presented a global analysis in order to compare mixing efficiency with different geometrical and physical parameters. Weetman and Oldshue (1988) compared the global parameters of this impeller to the A315 pitched-blade turbine (PBT) and a Rushton impeller under standard conditions. Zhou and Kresta (1996a,b) studied the maximum dissipation rate induced by different impellers (A310, PBT, Rushton) using laser Doppler anemometry (LDA) techniques. Ducoste et al. (1997) have analyzed A310 impeller effects on turbulence in flocculators.

In the first part of this article, the PIV technique principles are recalled. Then, the experimental facility is presented. The mean velocity field and the Reynolds stress components are analyzed in the case of the axially agitated tank. These data are then used to estimate the dissipation rate of the turbulent kinetic energy (TKE). The dissipation rate of TKE is deduced from the balance of TKE after estimating precisely the advection and production terms.

Experimental Study

PIV technique

The PIV system used in this study is a commercial system acquired from Dantec Measurement Technology. The principle of the PIV technique is presented below. Each data acquisition consists of an instantaneous two-dimensional (2-D) velocity field. If the displacement of fluid particles during a given time interval could be measured, then the velocity of the fluid particles could be estimated. Since water is transparent, the displacement of fluid particles cannot be observed. Therefore, it is necessary to seed the flow with small solid particles. Particles are distributed in the volume of the apparatus. In order to visualize particles located in the plane of the flow, a 2-D slice of the flow field is illuminated by a light sheet. The illuminated seeding scatters the light and is detected by a camera positioned perpendicular to the light sheet. The light sheet is quickly pulsed for a short time. This freezes the positions of the particles on the first frame of the camera. The camera frame is moved and a second camera frame is exposed to the light scattered by the particles from a second pulse of laser light. In this way, two camera images are recorded, the first showing the initial position of the seeding particles and the second their final position due to the motion of the fluid. The time between the recorded images (the same as that between the light-sheet pulses) is known. The two camera frames are then processed to determine the instantaneous velocity field. Each camera image is divided into small squared interrogation regions (32 or 64 pixels). In each interrogation region, the positions of all particles are detected and the displacement of the particles between frame 1 and frame 2 is measured using correlation methods. The velocity vector of this region is then calculated. This procedure is repeated for each interrogation region, thereby building up the whole 2-D velocity vector map.

The system used in this study includes a 4-W continuous-wave laser (Innova 70-4 from COHERENT, argon-ion source), an electrooptical shutter, an optical fiber, a polygon scanner, a double-image 700 recorder camera (CCD camera, 768−484 pixels), a dedicated processor (PIV 2000), and software. The pulsing light sheet is generated by a continuous-wave laser pulsed with the electrooptical shutter. The laser beam is transferred to the polygon scanner via the optical fiber. The polygon scanner generates a laser-illuminated slide in the flow. The recorder camera is interfaced with the processor. The processor makes all the calculations in real time. As the processor produces vector maps, these calculations are displayed and optionally stored by the software. The software also automatically generates all the synchronization signals for system integration. The seeding material is polyamid nylon 6 microparticles (density = 1.13, 5 μm $< d_p <$ 45 μm) or spherical, hollow, silvered glass particles from Dantec (density = 1.4, 10 μm $< d_p <$ 30 μm).

Experimental apparatus

The apparatus used in this study consists of a standard cylindrical tank with four baffles and a Lightnin A310 axial flow impeller. The cylindrical tank is made of glass (6 mm thick) with faces of $T = 45$ cm diameter and a liquid height of $H = T = 45$ cm. The cylindrical vessel is placed in a cubic tank filled with tap water to eliminate the laser-sheet refraction. Four equally spaced baffles are also made of glass (width $B = 4.5$ cm $= T/10$). The turbine has a standard design with a diameter of $D = T/3 = 15$ cm and a vertical position C equal to the diameter, measured from the tank bottom. The tank, filled with tap water as the working fluid, is open at the top, and the water height, H, is three times the impeller diameter ($H = 3D$). The impeller is centrally located and rotates at 200 rpm.

The ratio of the impeller diameter to the tank diameter is 1/3. The ratio of the height of the liquid to the tank ratio is 1. The ratio of the vertical position of the impeller, or clearance C, to the tank diameter T is $C/T = 1/3$. The impeller rotated in a clockwise direction, as viewed from above.

Given the impeller rotational speed, N, and the impeller diameter, D, the tip velocity can be estimated by

$$U_{\text{tip}} = \pi ND$$

Accuracy

The accuracy of the measurements depends on seeding concentration, the size of the PIV measurement area, the time interval between the two laser sheets, and on spatial resolution. Table 1 contains the PIV measurement conditions of our experiment. It must be pointed out that the time delays between laser flashes are adapted to local velocities. Indeed,

Table 1. Experimental Conditions in Tank

Kind of PIV Image	Large	Small
Size of image (cm)	23×17	6×4.8
Time delay between laser flashes (μs)	1,000	600
Time between two velocity field records (ms)	251	251
No. of pixels in each interrogation area	32	32
No. of events, NE	400	1,700
No. of vectors ($M \times N$)	47×29	47×29
Impeller	A310	A310
Rotation speed (tr/min)	200	200
Fluid	Water	Water

the values that are given in Table 1 are only given as an indication. Two different sizes of PIV measurement area have been used:

- A "large" PIV measurement area of 230×170 mm^2 has been used to determine the global circulation in the tank; in this case, the time delay between laser flashes in the impeller region was 1 ms; the size of the elementary window (or interrogation region) used to determine one velocity vector was then 6×6 mm^2.
- A "small" PIV measurement area of 60×48 mm^2 has been used to analyze the velocity and turbulence below the impeller; in this case, the time delay between laser flashes was 600 μs; the size of the elementary window (or interrogation region) used to determine one velocity vector was then 1.5×1.5 mm^2.

In each case, the seeding concentration was adapted in order to have between 5 and 10 particles in the elementary window (or interrogation region).

The time delay between laser flashes depends on local hydrodynamics. For example, in the case of the large PIV measurement area, the size of the elementary window was fixed at 6 mm; the tip velocity being close to 1.5 m/s, a time delay between the 1 ms laser flashes was chosen in this region, since it corresponds to a displacement of the particles equal to a quarter of the window size (1.5 mm).

The main problem is related to spatial resolution in order to avoid filtering in estimation of turbulent characteristics. Turbulence was determined for the small PIV measurement area, with characteristic measurement-area length scales equal to 60 mm and an elementary window (or interrogation region) equal to 1.5 mm. These length scales can be compared to the integral length scale, Λ, and to the Taylor microscale, λ. The integral length scale, Λ, can be estimated directly from PIV measurements. This has been done, but the detailed results are not reported in this article. Below the impeller, the integral length scale ranges between 5 mm and 10 mm. Between the impeller tip and the lateral wall, it ranges between 20 mm and 30 mm. Then the size of the 60×48 mm^2 measurement area seems reasonable. The Taylor microscale, λ, can be estimated from measurements that will be presented in a succeeding article. However, its order of magnitude can be given here. In isotropic turbulence, the Taylor microscale λ is

$$\lambda = \sqrt{\frac{15\nu\overline{u'^2}}{\epsilon}}$$

The velocity correlation can be estimated by $2/3\ k$, where k is the turbulent kinetic energy and ϵ is its dissipation rate. The order of magnitude of the Taylor microscale, λ, ranges between 1 mm and 2 mm, and then is equal or slightly larger than the size of the basic window.

Estimation of the average statistical data has been performed on a series of 1,700 instantaneous velocity fields. Statistical convergence has been checked both on mean velocity and Reynolds stress components.

In addition, so-called spurious vectors are encountered in PIV. In our experiments, these spurious vectors correspond to displacement vectors in the correlation plane with peak heights that are rejected. Indeed, the processor locates the highest and second highest peak in the correlation plane. These two peaks are compared, the highest peak must be 1.2 times larger than the second one. If the noise is too large, the vector is rejected. In the statistical averaging procedure, these spurious vectors were ignored and the statistical average was determined on a smaller number of data, which accounts for the missing data.

In our experiments, raw data were used as instantaneous velocity fields, without filtering and without move-averaging validation.

Reproducibility

The reproducibility of the measurements has been verified, since measurements have been performed in three perpendicular planes in order to determine the three components of the velocity and the six components of the Reynolds stress tensor: the first plane was necessary to measure U_1, U_2; the second plane was necessary to measure U_1, U_3; and the third plane was necessary to measure U_2, U_3. Hence, the data on the instantaneous velocity components were systematically performed using two different planes and the profiles were compared to validate the measurements.

Flow Field and Reynolds Stress Distribution

Mean flow properties

PIV measurements provide instantaneous velocity fields in a plane. In turbulent flow, it is necessary to average the instantaneous information over a large number of events in order to determine an averaged statistical value. The statistical average is defined as follows

$$\overline{U_i}(M, t) = \frac{1}{NE} \sum_{k=1}^{NE} U_i^k(M, t)$$

where NE corresponds to the number of events used in the statistical averaging. Following the Reynolds decomposition, each instantaneous component can be considered as the sum of the averaged component and a fluctuation

$$U_i^k(M, t) = \overline{U_i}(M, t) + u_i'^k(M, t)$$

This decomposition allows the estimation of the mean velocity field and the distribution of the Reynolds stresses, defined as

$$\overline{u_i' u_j'}(M, t) = \frac{1}{NE} \sum_{k=1}^{NE} u_i'^k(M, t)\, u_j'^k(M, t)$$

The mean values in a turbulent flow are then the three components of the mean velocity and the six components of the symmetrical Reynolds tensor.

First it was necessary to validate the measurements before applying them to the mixing tank (Bugay, 1998). In the case of a fully developed turbulent pipe flow, the flow field and turbulence measurements were validated by comparison to different data [experimental data after Laufer (1954), and numerical data after Eggels et al. (1994)]. Two Reynolds numbers were investigated (6,500 and 20,000). The data acquired at the lower Reynolds number were compared to the data of Eggels et al. (1994), and the data acquired at the larger Reynolds number were compared to the data of Laufer (1954). The comparisons validated the measurement of the turbulent flow characteristics.

The PIV technique was then applied to measure the mean velocity field in the agitated tank. An averaged velocity field is plotted on Figure 1, in a vertical plane of symmetry in the tank. The vertical plane is a bisector plane relative to two baffles. The axial flow structure is clearly shown. As far as global circulation of the mean flow is concerned, it is not necessary to investigate the velocity field in detail. Consequently, the tank's vertical plane of symmetry was divided into three sections. The velocity field in each section of this plane was obtained after PIV measurements from images in the plane (x_1,x_3). The size of each PIV measurement area was 230 mm $\times$ 170 mm (see Figure 2a and Table 1, column Large PIV image). The number of velocity vectors was 47 in the radial direction and 87 (3×29) in the vertical direction. This number corresponds to one vector each 5 mm in both directions. Three circulation loops can be seen in Figure 1. The main circulation loop almost fills the whole tank. It is generated by the axial flow impeller. Maximum velocities are located near the impeller and close to the lateral wall of the tank. A secondary circulation loop is located at the bottom of the tank, below the impeller shaft. It is generated by the jet induced by the impeller, impinging on the bottom of the tank. A third circulation loop is located just below the free surface, close to the lateral wall, and the magnitude of its velocity is low.

In order to estimate both mean values and turbulent fluctuations, it was necessary to measure the velocity fields on smaller images. Measurements were carried out for a large number of small images to determine the three components of the instantaneous velocity field in a vertical plane of the tank. The size of each image was 60 mm $\times$ 48 mm. The whole plane located below the impeller was investigated ($0 < x_1 < R_{\text{tank}} = 22.5$ mm in the radial direction; $0 < x_3 < Y = 145$ mm in the vertical or axial direction). PIV measurement locations are shown in Figures 2b to 2d. Since the number of velocity vectors in the radial direction on each image is 47, the total corresponds to one vector each 1.5 mm. In the case where the number of velocity vectors in the vertical direction on each image is 29, the total corresponds to one vector each 1.5 mm, too. Experimental conditions are given in Table 1.

From this velocity field in a plane, it is possible to plot radial profiles of velocity components at different vertical positions, above and below the impeller. Since it is the impeller that drives the flow, a local measurement of the impeller discharge is needed. The radial profiles of the three components of the velocity field just below the impeller are plotted in Figure 3b. It is then possible to estimate global information such as the pumping flow rate, Q_p, corresponding to the type of impeller and to the rotational speed N

$$Q_p = \frac{2}{R^2}\int_0^R \overline{U_3}(r)\,r\,dr$$

where the subscript 3 corresponds to the downward vertical coordinate and R is the radius of the impeller ($R = D/2$).

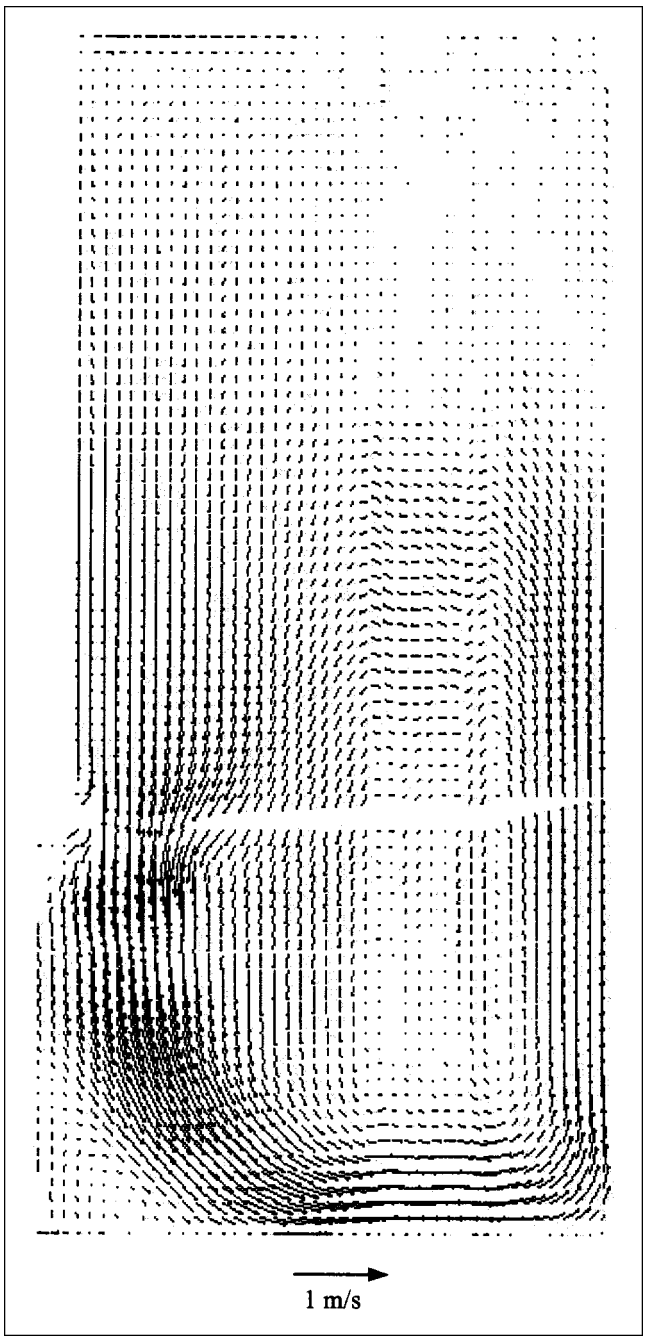

Figure 1. Mean velocity in a vertical plane in the agitated tank.

The pumping number can then be estimated as

$$N_{Q_p} = \frac{Q_p}{ND^3}$$

From our experimental results, the pumping number of the A310 impeller is estimated to be 0.55, which is close to the values 0.62 from Mavros et al. (1996) and 0.56 from Weetman and Oldshue (1988).

The turbulent flow induced by an axial flow impeller has some original features that can be highlighted, using the mean velocity variation and higher moments in the whole tank, above and below the impeller.

In practice, the velocity is nondimensionalized as follows

$$U_i^* = \frac{\overline{U_i}}{U_{\text{tip}}}$$

The impeller is located at a level of 150 mm from the bottom of the tank. The velocity components were measured at three levels above the impeller ($X_3 = 440$ mm, 300 mm, and 180 mm) and 13 levels below the impeller (145 mm $> X_3 >$ 25 mm). The three profiles plotted in Figures 3a to 3c correspond, respectively, to (a): 440 mm; (b): 145 mm; and (c): 65 mm.

The profile plotted in Figure 3b is located just 5 mm below the impeller. The vertical flow is pumped downward by the axial flow impeller ($\overline{U_3} < 0$, $r/R < 1$, below the impeller) and flows upward along the lateral wall ($\overline{U_3} > 0$, $r/R > 2.2$). The axial velocity magnitude reaches 30% of the tip impeller velocity at $r/R = 0.6$. The radial velocity magnitude ($\overline{U_1}$) is small. Below the impeller, the tangential velocity ($\overline{U_2}$) ranges between 30 and 50% of the longitudinal velocity and corresponds to 10% of the tip velocity.

Above the impeller (Figure 3a), the axial velocity remains larger than the two other components. Velocity magnitude

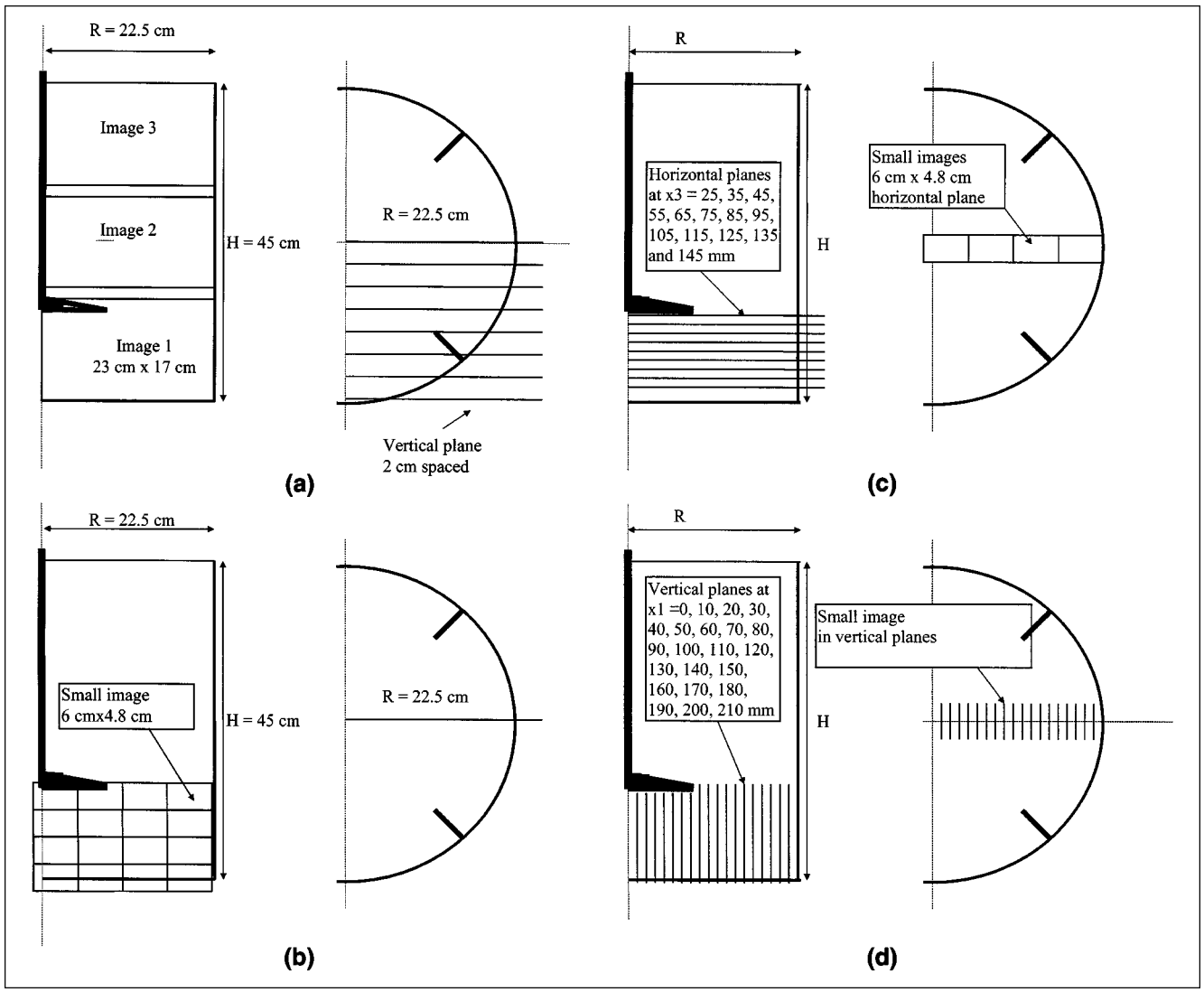

Figure 2. Tank and impeller.

(a) Large PIV images; (b) small PIV images to measure $\overline{U_1}$, $\overline{U_3}$, $\overline{u_1'^2}$, $\overline{u_3'^2}$, and $\overline{u_1'u_3'}$; (c) small PIV images to measure $\overline{U_1}$, $\overline{U_2}$, $\overline{u_1'^2}$, $\overline{u_2'^2}$, and $\overline{u_1'u_3'}$; (d) small PIV images to measure $\overline{U_2}$, $\overline{U_3}$, $\overline{u_2'^2}$, $\overline{u_3'^2}$, and $\overline{u_2'u_3'}$.

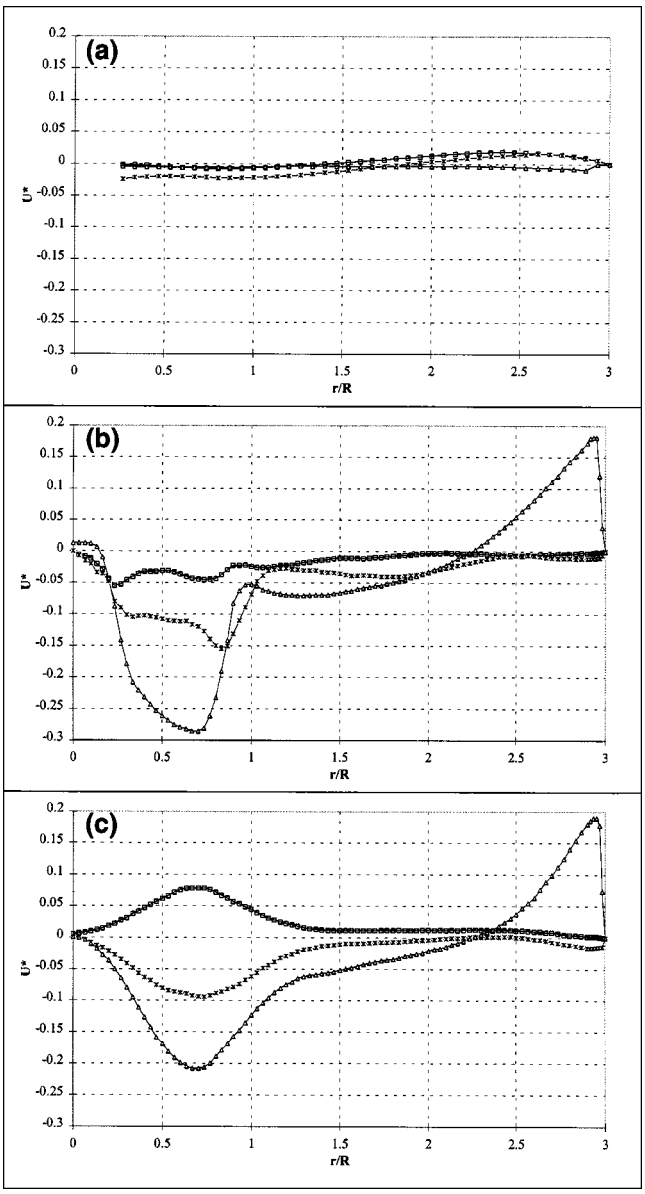

Figure 3. Radial profile of mean velocity (□: U_1^*; ∗: U_2^*; Δ: U_3^*).

(a) $X_3 = 440$ mm (10 mm below free surface); (b) $X_3 = 145$ mm (5 mm below impeller position); (c) $X_3 = 65$ mm.

decreases near the free surface, where the axial velocity is negligible. One can observe two horizontal circulation loops. In the center part of the free surface ($r/R < 1.5$), the liquid rotates in the same way as the impeller; close to the tank wall ($r/R > 1.5$), the liquid rotation is opposite to that of the impeller.

Below the impeller (Figure 3b), the axial velocity maxima decrease (at 145 mm from the bottom, $U_3^* = 30\%$ at $r/R = 50\%$) toward the bottom (Figure 3c) (at 65 mm from the bottom, $U_3^* = 20\%$ at $r/R = 100\%$), under the influence of jet expansion, turbulent diffusion, and flow confinement. The radial profile of the axial velocity varies below the impeller due to the second circulation loop generated at the bottom below the impeller shaft. Below the impeller, the magnitude of radial velocity is small, except near the lower wall, due to the impact of the jet induced by the impeller. However, the tangential velocity is large: $U_2^* = 10\text{–}15\%$.

Reynolds stress tensor components

The measurement of the diagonal and nondiagonal Reynolds stress tensor components were first determined in turbulent pipe flow. The good agreement between our data and the data of Eggels et al. and Laufer validated the measurement of turbulent kinetic energy using the PIV technique. This means that the spatial filter associated with the small interrogation area of the PIV does not induce any significant bias in our measurements. In other words, the filtered scales of turbulent motions are not significantly energetic.

Diagonal Components in a Stirred Tank. The mixing can be quantified by the local turbulent kinetic energy, defined as

$$k = \frac{1}{2}\left(\overline{u_1'^2} + \overline{u_2'^2} + \overline{u_3'^2}\right)$$

corresponding to the half-trace of the Reynolds stress tensor. Experimentally, each normal component of the Reynolds tensor is determined separately.

Normal stresses are nondimensionalized, as

$$u_i^* = \frac{\sqrt{\overline{u_i'^2}}}{U_{\text{tip}}} \quad \text{and} \quad k^* = \frac{\sqrt{k}}{U_{\text{tip}}}$$

The normal stresses and TKE were measured at three levels above the impeller (440 mm, 300 mm, and 180 mm) and 13 levels below the impeller (145 mm $> X_3 >$ 25 mm). For the sake of simplicity, the normal stresses and TKE profiles are plotted at three levels in Figures 4a to 4c (a: 440 mm; b: 145 mm; c: 65 mm). Below the impeller (Figure 4b), two peaks of TKE appear: the maximum one ($k^* = 0.11$) is generated by the impeller (at $r/R = 80\%$), and the second one ($k^* = 0.09$) is generated by the shear flow along the impeller axis ($r/R = 25\%$). The two peaks collapse at 45 mm from the bottom. The radial profiles of these components between the impeller tip ($r/R = 1$) and the lateral wall ($r/R = 3$) are flat and have an approximately constant value ($k^* = 0.04$), which corresponds to isotropic turbulence. Just below the free surface (Figure 4a), the normal vertical (or axial) stress decreases in comparison to the two other components. The normal tangential stress dominates. It corresponds to 2-D turbulence.

Turbulent kinetic energy is drawn in a vertical plane in the lower part of the vessel (Figure 5a). The vertical profiles of TKE have been plotted in Figure 5b. In the impeller vicinity at given radial positions, these figures show that the TKE is

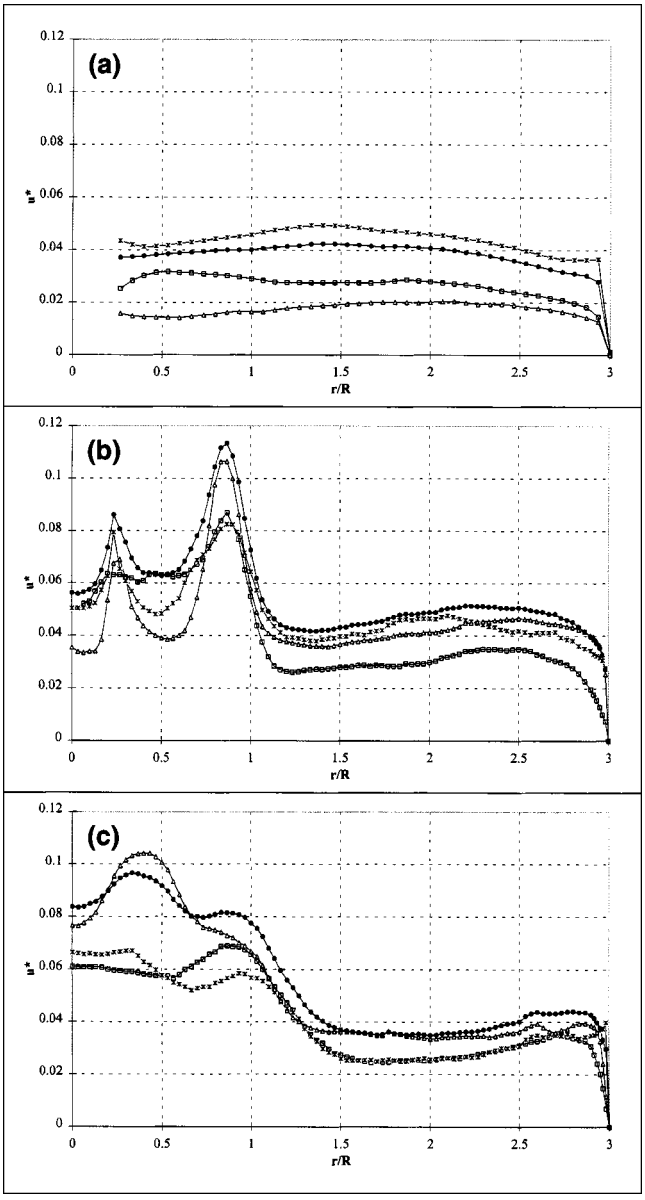

Figure 4. Radial profile of diagonal components of Reynolds tensor and turbulent kinetic energy (□: u_1^*, ∗: u_2^*; Δ: u_3^*; ●: k^*).

(a) $X_3 = 440$ mm; (b) $X_3 = 145$ mm; (c) $X_3 = 65$ mm.

generated by the impeller, for radial positions at $r/R = 0.2$ and $r/R = 0.8$. For these radial positions, the TKE level decreases strongly below the impeller. In the region closer to the axis of symmetry, the TKE is generated locally by the circulation loop below the shaft of the impeller.

Nondiagonal Components in a Stirred Tank. The three nondiagonal Reynolds stress components were also measured at 16 levels. Only three radial profiles are plotted in Figures 6a to 6c (a: 440 mm; b: 145 mm; c: 65 mm). The radial profiles of these components are flat and close to zero between the impeller tip ($r/R = 1$) and the lateral wall ($r/R = 3$). Below the impeller, Figure 6b, the maximum shear corresponds to the axial–tangential turbulent velocity correlation. Below the impeller, Figure 6c, the maximum shear stress corresponds to the axial–radial turbulent velocity correlation, generated by the circulation loop of the mean velocity field below the impeller. Above the impeller, Figure 6a, the magnitude of the shear stress components is small.

Dissipation Rate of TKE

Previously estimated TKE dissipation rate just below the impeller

The mean-velocity radial profiles and Reynolds stress components plotted just below the impeller are useful for determining boundary conditions in CFD simulations. The other profiles constitute a data bank to test the validity of turbulence models used in CFD codes.

Indeed, a major problem using a single-point closure model in CFD modeling is related to the determination of the rate of dissipation of turbulent kinetic energy. Many authors have proposed estimating the TKE dissipation rate below the impeller by assuming that it is related to the turbulent kinetic energy k and to a macro length scale Λ as

$$\epsilon = C\frac{k^{3/2}}{\Lambda} \quad \text{with} \quad \Lambda(D)$$

where the macroscale is seen as a linear function of the impeller diameter D. This relation is based on the argument that the energy content can be characterized by k, its rate of transfer by $k^{1/2}$ over Λ. The turbulent kinetic energy is transferred from mean flow to large-scale motions, as most of the turbulent energy is contained in large eddies; the turbulent kinetic energy is dissipated by viscous dissipation of the small-scale motions, the energy cascade transfer occurring without dissipation. In the literature, the macroscale Λ below the impeller is assumed to be constant for a given impeller.

The constant, C, is known to be close to 1 in isotropic turbulence. In nonisotropic flow, different constant values have been proposed, which results in a wide variation in the estimated dissipation rate.

If we assume a constant ratio D/Λ and if we consider the experimental profile of turbulent kinetic energy, the resulting dissipation rate profiles can be estimated. Following Zhou and Kresta (1996), the dissipation rate can be determined by

$$\epsilon = 10\frac{\left(\overline{u_3'^2}\right)^{3/2}}{D}$$

which corresponds to D/Λ equal to 10.

In fact, such an estimation of the macroscale can have some shortcomings. In his doctoral thesis, Michelet (1998) brought interesting arguments to bear on the discussion of this problem in the case of a Rushton turbine. Here his arguments are adapted to the case of the axial flow impeller Lightnin A310. The maximum TKE below the impeller is located at $r/R = 0.8$ and is given by

$$\frac{\sqrt{k}}{\pi ND} = 10\%$$

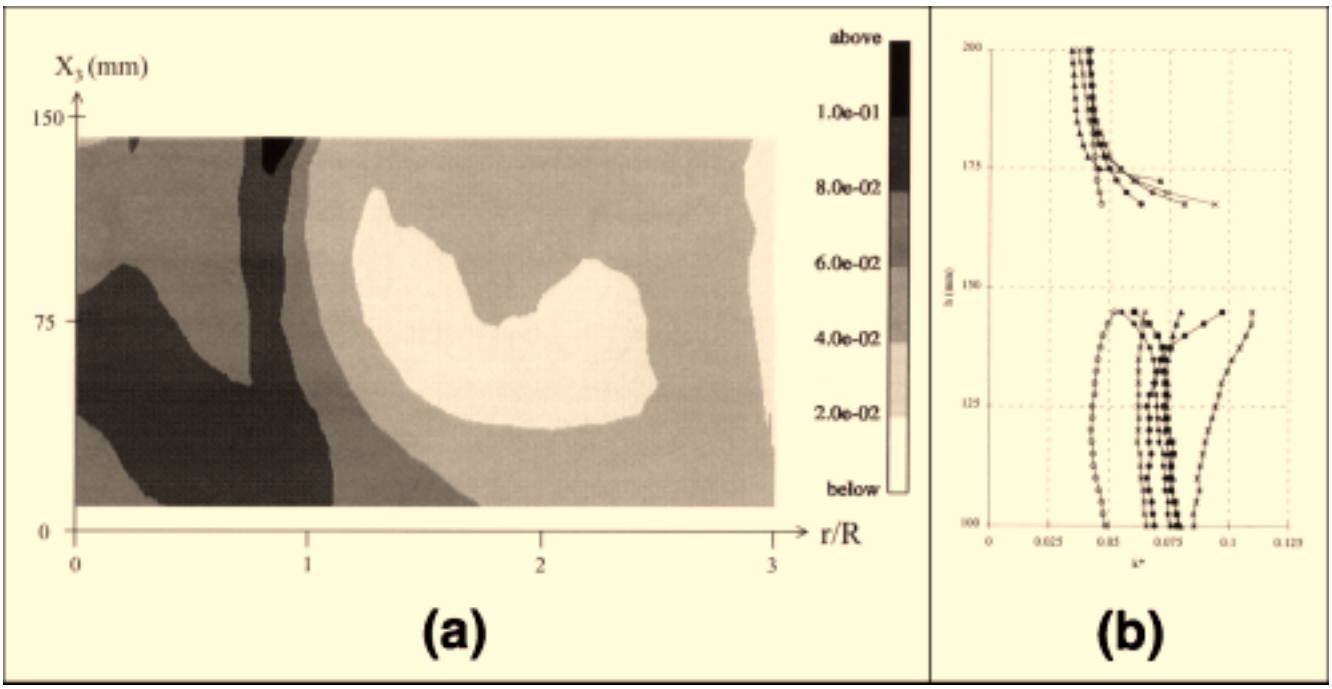

Figure 5. Turbulent kinetic energy in the agitated tank.

(a) Turbulent kinetic energy in vertical plane; (b) vertical profile of TKE in impeller vicinity (♦: $r/R = 0$; ■: $r/R = 0.13$; ▲: $r/R = 0.27$; ×: $r/R = 0.53$; ∗: $r/R = 0.67$; ●: $r/R = 0.93$; ○: $r/R = 1.07$).

If the previous integral macroscale is taken, $\Lambda = D/10$, then the characteristic time to turbulence equilibrium is given by $L/\sqrt{k}$, which corresponds to a time interval of 0.1 s. In addition, in this region the vertical velocity component reaches

$$\frac{U_3}{\pi ND} = 25\%$$

so the distance over which turbulence has been transported by the mean flow (during 0.1 s) is roughly equal to 40 mm, which is large compared to the distance between the impeller and the bottom of the tank. This means that the turbulence, generated in the region of the impeller, has been transported over a large distance during the time needed for the turbulence to develop.

In addition, if we perform the same analysis closer to the impeller shaft ($r/R = 0.5$), the TKE is not maximum and can be estimated as

$$\frac{\sqrt{k}}{\pi ND} = 5\%$$

The vertical velocity being nearly uniform below the impeller, the turbulence is developed when it has been transported over a distance of 100 mm. The application of the "classic" relation previously used to estimate the dissipation rate of TKE, and given as follows

$$\epsilon = C\frac{k^{3/2}}{\Lambda} \quad \text{with} \quad \Lambda(D)$$

is then questionable.

Newly estimated TKE dissipation rate just below the impeller

In the present study, the three components of the mean velocity field and the six components of the Reynolds stress components were precisely determined, particularly in the region of the impeller. These data can be used to estimate the dissipation rate of TKE, based on the balance equation of the TKE. The dissipation rate of TKE can be deduced from the balance of the TKE after estimating the advection and production terms.

The transport equation of TKE is classically expressed as follows

$$\frac{\partial k}{\partial t} + \frac{\partial k\overline{U_j}}{\partial x_j} = \frac{\partial}{\partial x_j}\left[\nu\frac{\partial k}{\partial x_j} - \overline{u_j'\left(\frac{p'}{\rho} + \frac{u_i'u_i'}{2}\right)}\right] - \overline{u_i'u_j'}\frac{\partial \overline{U_i}}{\partial x_j} - \epsilon$$

The flow is steady state, and the diffusion term can be neglected in comparison to those of advection and production. The balance equation of TKE reduces then to

$$\epsilon = -\overline{u_i'u_j'}\frac{\partial \overline{U_i}}{\partial x_j} - \frac{\partial k\overline{U_j}}{\partial x_j}$$

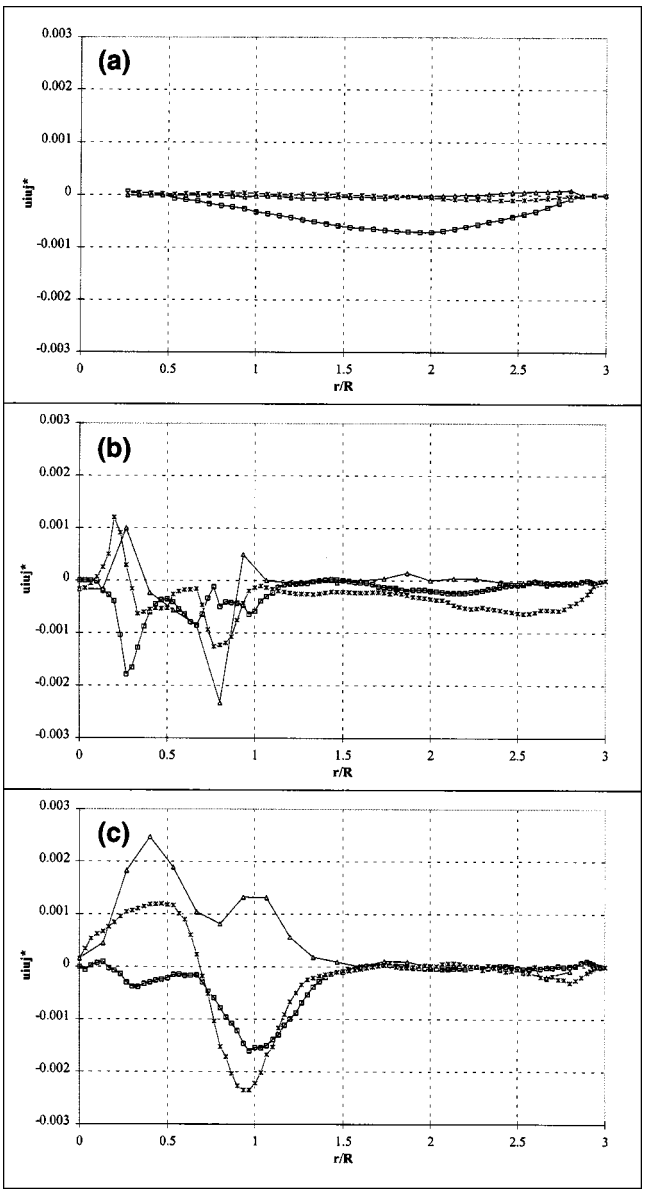

Figure 6. Radial profile of nondiagonal components of Reynolds tensor of turbulent kinetic energy (□: $u_1u_2^*$; ∗: $u_1u_3^*$; Δ: $u_2u_3^*$).

(a) $X_3 = 440$ mm; (b) $X_3 = 145$ mm; (c) $X_3 = 65$ mm.

The three terms of advection and nine terms of production of the TKE were estimated directly from experiments.

Among the three terms of advection, the term corresponding to the vertical transport is the most significant. Below the impeller, the vertical velocity is negative (downward flow) for $0.2 < r/R < 1$; in this region, the vertical profiles of the TKE were plotted in Figure 5. The vertical gradient of TKE below the impeller is positive. This leads to a negative TKE transport term. Closer to the axis of symmetry, the vertical velocity is positive (upward flow) and, in this region, the vertical gradient of the TKE is negative (Figure 5). This also leads to a negative transport term of the TKE. It is very interesting to note from Figure 7 that this TKE transport term almost balances the dissipation rate of the TKE for $0.25 < r/R < 0.75$, since the production of the TKE is negligible in this region. Just below the impeller, the contribution of the production of the TKE is then limited to the regions corresponding to the two peaks of the TKE at $r/R = 0.2$ and $r/R = 0.8$, which is obvious.

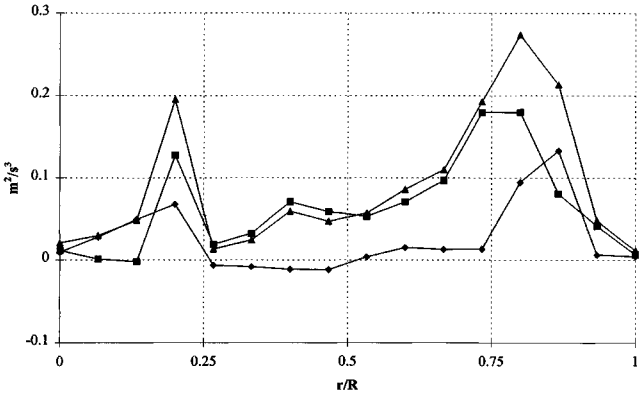

Figure 7. Radial profile of turbulent kinetic energy balance below the impeller ($X_3 = 145$ mm) (♦: production term; ■: transport term; ▲: dissipation rate).

Outside the regions of the production of the TKE, the global circulation loop transports TKE, and one obtains an equilibrium between the transport and dissipation of TKE. In the region of the impeller tip (at $r/R = 0.8$, for example), the impeller produces turbulence. Locally, there is an equilibrium between production, transport and dissipation of TKE.

The production of TKE results from nine terms. Among these nine terms (Figure 8), the main contributions just below the impeller are a function of the following three terms

$$-\overline{u_1'u_3'}\frac{\partial \overline{U_3}}{\partial x_1}, \quad -\overline{u_3'^2}\frac{\partial \overline{U_3}}{\partial x_3} \quad \text{and} \quad -\overline{u_1'^2}\frac{\partial \overline{U_1}}{\partial x_1}$$

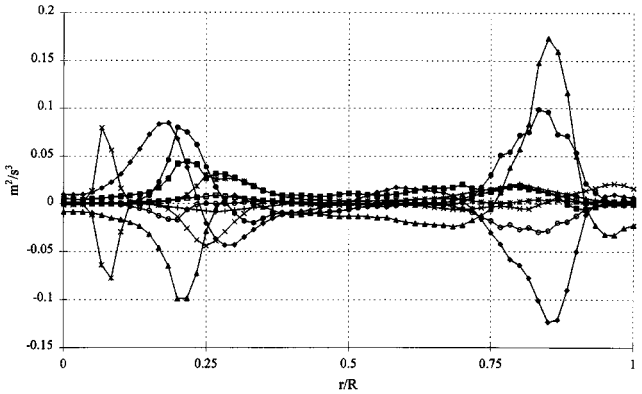

Figure 8. Radial profile of production terms of turbulent kinetic energy below the impeller ($X_3 = 145$ mm) [♦: $prod_{11}$; ■: $prod_{22}$; ▲: $prod_{33}$; × $prod_{21}$; ∗: $prod_{12}$; ●: $prod_{31}$; ○: $prod_{13}$; □: $prod_{32}$; +: $prod_{23}$ with $prod_{ij} = -u_i'u_j'(\partial \overline{U}_i/\partial x_j)$].

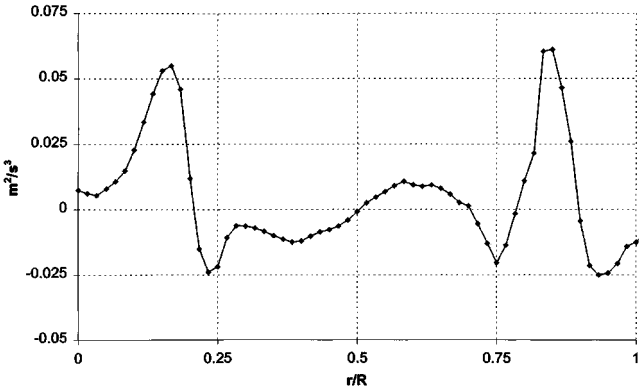

Figure 9. Radial profile of the sum of diagonal production terms below the impeller ($X_3 = 145$ mm).

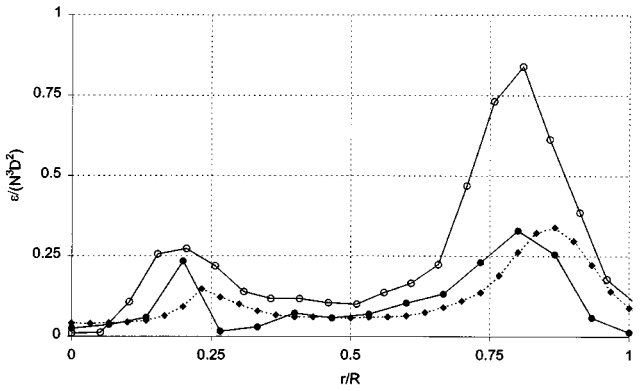

Figure 10. Radial profile of turbulent kinetic energy dissipation rate below the impeller ($X_3 = 145$ mm) (○: Zhou and Kresta (1996a); ●: turbulent kinetic energy balance; ♦: $\Lambda = D/7.5$).

Different interpretations can been made. If we plot the sum of the three "diagonal" terms of production just below the impeller in Figure 9

$$-\overline{u_1'^2}\frac{\partial \overline{U_1}}{\partial x_1} - \overline{u_2'^2}\frac{\partial \overline{U_2}}{\partial x_2} - \overline{u_3'^2}\frac{\partial \overline{U_3}}{\partial x_3}$$

we can see that it is not equal to zero. It should be equal to zero if the turbulence was isotropic. Consequently, it means that the turbulence is nonisotropic in the regions of heavy production of TKE, close to the two peaks of the TKE at $r/R = 0.2$ and $r/R = 0.8$.

In Figure 8, one can see that the production of TKE is significant in the regions corresponding to the peaks of TKE (at $r/R = 0.2$ and $r/R = 0.8$). Some terms of production of TKE are positive, others are negative, which can be easily understood. For example, at $r/R = 0.8$, the production terms $-\overline{u_1'u_3'}(\partial \overline{U_3}/\partial x_1)$, $-\overline{u_3'^2}(\partial \overline{U_3}/\partial x_3)$ are positive, and the production term $-\overline{u_1'^2}(\partial \overline{U_1}/\partial x_1)$ is negative. In fact, at $r/R = 0.8$, we can see in Figure 3b that $\partial \overline{U_1}/\partial x_1$ is positive, the radial velocity increasing with increasing radial distance. This explains why the production term $-\overline{u_1'^2}(\partial \overline{U_1}/\partial x_1)$ is negative. Due to incompressibility, $\partial \overline{U_3}/\partial x_3$ must be negative; therefore, the production term $-\overline{u_3'^2}(\partial \overline{U_3}/\partial x_3)$ is positive.

The main TKE production term is $-\overline{u_1'u_3'}\,(\partial \overline{U_3}/\partial x_1)$. The production of TKE is thus induced by the radial gradients of axial velocity. In fact, the impeller pumps the liquid downward, so there is a strong radial gradient of vertical velocity close to the tip of the impeller, with downward flow inside the impeller and an upward flow outside it.

Concerning the peak of the TKE located at $r/R = 0.2$, there is a strong radial gradient of vertical velocity close to the shaft of the impeller, with downward flow below the impeller and upward flow below its shaft. This leads to the positive production of turbulence induced by $-\overline{u_1'u_3'}(\partial \overline{U_3}/\partial x_1)$. In this region, $-\overline{u_1'^2}(\partial \overline{U_1}/\partial x_1)$ is positive, since the radial velocity decreases with increasing radial distance (see Figure 3b); hence $\partial \overline{U_1}/\partial x_1$ is negative. Due to incompressibility, $\partial \overline{U_3}/\partial x_3$ is positive, and so the production term $-\overline{u_3'^2}(\partial \overline{U_3}/\partial x_3)$ is negative.

Given the balance of the TKE just below the impeller, the resulting profile of dissipation rate of TKE is as shown in Figure 10 and compared to the Zhou and Kresta profile. There is some difference between the two profiles. Indeed, the present profile of dissipation rate of TKE could be better estimated by D/Λ equal to 7.5.

Estimated TKE dissipation rate far from the impeller

The analysis of the dissipation rate of the TKE just below the impeller was completed by the estimation of the dissipation rate at different levels in the tank. The terms accounting for the production and transport of the TKE were determined experimentally at six levels below the impeller. The profiles of the production, transport, and dissipation of the TKE were plotted, respectively, in Figure 11a, 11b, and 11c.

The production is globally positive. At $r/R = 0.8$, the TKE production peak is large just below the impeller (at 145 mm above the bottom or 5 mm below the impeller). The magnitude of the peak decreases continuously as the distance from the impeller increases. The impeller induces a liquid jet. This jet opens out, the radial gradients decrease, and the production of TKE decreases, too. It is interesting to note that when the TKE production peak decreases at $r/R = 0.8$, the production peak of TKE increases at r/R values between 0.2 and 0.3. This production is controlled by the recirculation loop located at the bottom of the tank and induced by the impinging jet.

The transport of TKE by the mean flow is never negligible. The radial profile of transport TKE varies rapidly below the impeller toward the bottom of the tank.

Neglecting the diffusion of TKE, one can estimate the profiles of the TKE dissipation rate (Figure 11c).

Dissipation rate of TKE in the region of the impeller

It is interesting to try to understand the exchange of energy in the region of the impeller. Following Cutter (1966) and Zhou and Kresta (1996b), the macroscopic energy balance equation, averaged on a control volume, can be written as follows

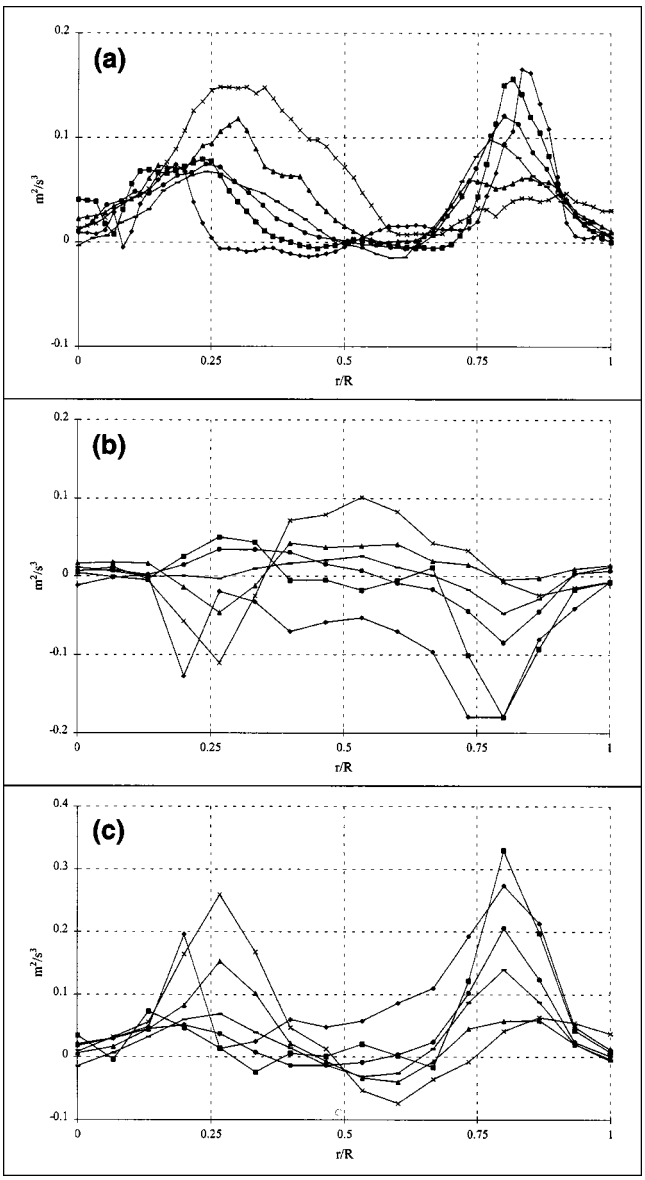

Figure 11. Balance of turbulent kinetic energy at different levels below the impeller (♦: $X_3 = 145$ mm; ■: $X_3 = 135$ mm; ●: $X_3 = 125$ mm; ———: $X_3 = 115$ mm; ▲: $X_3 = 95$ mm; ×: $X_3 = 75$ mm).

(a) Radial profiles of production term; (b) radial profiles of transport term; (c) radial profiles of dissipation rate.

$$\rho V_{\text{control}} \langle \epsilon \rangle_{V\text{control}} = P - \int_{\text{Contour}V} \rho \quad (\bar{K} + k) \quad V \cdot n \quad ds$$

Referring to our experiments, the control volume around the impeller is bounded by an upper horizontal plane just above the impeller (located at 180 mm) and by a lower horizontal plane just below the impeller (located at 145 mm). The height (h) of the control volume is then 35 mm. The horizontal surface of the volume corresponds to the disk described by the impeller

$$V_{\text{control}} = \frac{\pi D^2}{4} h = 6.2 \times 10^{-4}\,\text{m}^3$$

The term on the lefthand side of the macroscopic balance represents the rate of viscous dissipation of both the mean ($\bar{K}$) and turbulent (k) kinetic energy; the first term on the righthand side, P, represents the rate at which the work of the stresses distributed on the surface of the impeller blades enters the control volume. The axial flow impeller Lightnin A310 has a power number N_P equal to 0.3. We define N_P as follows

$$N_P = \frac{P}{\rho N^3 D^5}$$

where P is the power input. The amount of power is closely related to the turbulence in the tank. In our case ($D = 0.15$ m and $N = 200$ rpm $= 3.33$ s^{-1}), it corresponds to $P = 0.8$ kg·m^2/s^3 $= 0.8$ W.

The volume of liquid in the tank is given by

$$\vartheta = \pi \frac{T^2}{4} H = \frac{27\pi}{4} D_3$$

This corresponds to a volume of 0.07 m^3 = 70 L. Thus, the dissipation rate of TKE for unit volume is given by

$$\langle \epsilon \rangle_{\text{tank}} = \frac{P}{\rho \vartheta} = 0.012\ \text{m}^2/\text{s}^3$$

The second term on the righthand side represents the transport of mean ($\bar{K}$) and turbulent (k) kinetic energy by the mean flow field, through the boundary of the control volume. The fluid that transports the kinetic energy mainly enters the control volume through the upper surface with a vertical downward velocity and flows out of the control volume through the lower surface with a vertical downward velocity. We can estimate from experiments the flux of mean ($\bar{K}$) and turbulent (k) kinetic energy through each surface of the control volume (Table 2).

Thus, the kinetic energy entering the control volume represents 0.1 W and the kinetic energy flowing outwards represents almost 0.6 W. Recall that the power input P is equal to 0.8 W. Two conclusions can be drawn:

- First, the energy dissipated inside the control volume around the impeller is equal to 0.3 W; it represents 40% of the power input, which is equal to the total rate of energy dissipated in the tank. Consequently, 60% of the kinetic energy seems to be dissipated outside the control volume, far from the impeller region, probably in the regions close to the baffles of the tank.
- Second, the radial profile of dissipation rate of TKE was plotted in Figure 10 just below the impeller. From this pro-

Table 2. Transport of Kinetic Energy

Upper Surface	Lower Surface	Upper Surface	Lower Surface
0.08 W	0.5 W	0.02 W	0.09 W
Transport of K Through		Transport of K Through	

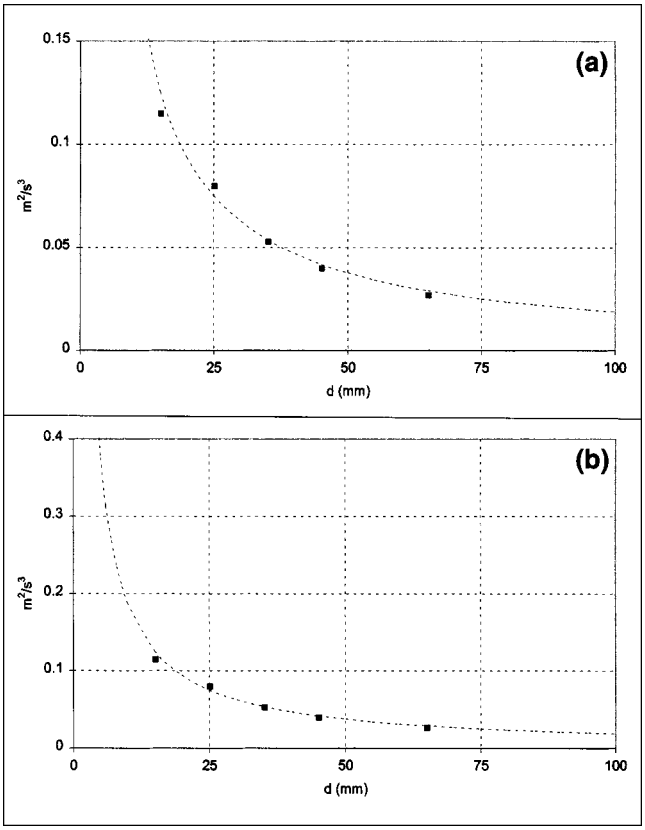

Figure 12. Vertical profile of $\langle \epsilon \rangle_{\text{projected surface}}$ below the impeller (■: experiment; ···: model).

(a) Region below the impeller; (b) Extrapolation into impeller region.

file, one can estimate the average dissipation rate of TKE below the impeller

$$\langle \epsilon \rangle_{\text{impeller}} = \frac{2}{R^2} \int_0^R \epsilon(r) r dr = 0.115 \text{ m}^2/\text{s}^3$$

This is small compared to the average energy dissipated in the control volume, which can be estimated from the macroscopic balance of energy and given by

$$\langle \epsilon \rangle_{V\text{control}} = 0.5 \text{ m}^2/\text{s}^3$$

Indeed, this result can be understood by plotting, below the impeller, the vertical profile of the dissipation rate of TKE averaged over the projected surface of the impeller (Figure 12a and 12b). In Figure 12, the average values of the TKE dissipation rate has been plotted vs. a distance between the measurement plane and a reference plane taken at the 160 mm level. One can see that the estimations of the average values of the TKE dissipation rate greatly increase when the distance d from the impeller decreases. One can fit the points of Figure 12a with a curve expressed as follows

$$\langle \epsilon \rangle_{\text{projected surface}}(d) = \frac{1.88}{d}$$

By extrapolating the curve in the region of the impeller (Figure 12b), one can observe that the magnitude of the TKE dissipation rate reaches values that are consistent with the aforementioned value of average energy dissipated in the control volume that was estimated from the macroscopic balance of energy around 0.5 m^2/s^3.

In conclusion, the impeller transmits a power P of 0.8 W to the mean flow through the work of the stresses exerted on its surface. The global circulation input to the region of the impeller is 0.08 W by the advective transport of the kinetic energy ($\bar{K}$) of the mean flow. This circulation output of the impeller region is 0.5 W, also by advective transport. Consequently, in terms of the production of TKE, 0.38 W has been transferred by the mean flow to the turbulence.

Concerning the turbulence, the global circulation input to the region of the impeller is 0.02 W by the advective transport of turbulent kinetic energy (k). This circulation output of the impeller region is 0.1 W, also by advective transport. The TKE receives 0.38 W in terms of the production of TKE by the mean flow. Consequently, 0.3 W has been dissipated by the viscosity in the region of the impeller.

The dissipation rate of TKE seems to be very high in the impeller region. It decreases rapidly with distance from the impeller. Estimation of the TKE dissipation rate just below the impeller by measuring the mean velocity and Reynolds stresses shows that the level of the TKE dissipation rate in this plane is relatively small compared to the estimated level closer to the impeller.

Summary and Conclusion

The mean velocity and turbulent characteristics of the flow induced by an axial flow impeller (Lightnin A310) have been presented in this article. The PIV technique has been used to improve the knowledge of the flow structure in the agitated tank.

The present results have significant implications for a better understanding of the local phenomena as well as for computational modeling: these results improve the knowledge of the boundary conditions to be imposed below the impeller and they provide reliable data banks to test and validate the modeling of turbulence and mixing in stirred tanks.

One of the main problems in mixing is related to the turbulent kinetic energy dissipation rate. This dissipation rate cannot be measured directly. Consequently, we have proposed that this dissipation rate be deduced from measuring the local mean flow and turbulence components. Both the production of TKE and the advective transport of TKE were estimated after experiments. The radial profile of the dissipation rate below the impeller was then derived from the local balance of turbulent kinetic energy.

The dissipation-rate profile of the TKE is compared to the TKE dissipation rate estimated by correlations

$$\epsilon = C \frac{k^{3/2}}{\Lambda} \quad \text{with} \quad \Lambda(D)$$

with a constant ratio D/Λ. The present work leads to $D/\Lambda = 7.5$. Since such a relation remains questionable, we recommend using the dissipation-rate profile of the TKE derived from the local balance of TKE.

In the last part of the article, it was shown that the energy dissipated around the impeller represents 40% of the power input. Consequently, 60% of the kinetic energy is dissipated outside the impeller region. In addition, the estimation of the vertical profile of the TKE dissipation rate averaged over the projected surface of the impeller exhibits a rapid increase as the distance d from the impeller decreases. This observation explains why the average TKE dissipation rate below the impeller ($\langle \epsilon \rangle_{\text{impeller}} = 0.115\ \text{m}^2/\text{s}^3$) is small compared to the average energy dissipated in the control volume, which has been estimated from the macroscopic balance of energy in the region of the impeller ($\langle \epsilon \rangle_{V\text{control}} = 0.5\ \text{m}^2/\text{s}^3$). By extrapolating the vertical profile of the TKE dissipation rate in the region of the impeller, one can observe that the magnitude of the TKE dissipation rate reaches high values that are close to the aforementioned value of the average energy dissipated in the control volume that was estimated from the macroscopic balance of energy.

Acknowledgment

The financial support provided by Ministère de l'Education Nationale et de la Recherche, Région Midi-Pyrénées and CIRSEE-Suez-Lyonnaise des Eaux is gratefully acknowledged.

Notation

B = blade width, m
C = impeller clearance, m
d = distance between measurement point and reference point, mm
D = impeller diameter, m
d_p = seeding particle diameter, m
H = liquid height in the tank, m
k = turbulent kinetic energy, m^2/s^2
K = mean kinetic energy, m^2/s^2
N = rotational speed, rev/s
N_P = power number
N_{Q_p} = pumping number
P = power input
Prod = production of turbulent kinetic energy, m^2/s^3
Q_p = pumping flow, m^3/s
R = impeller radius, m
R_{tank} = tank radius, m
Re = Reynolds number
T = tank diameter, m
U,u = velocity component, m/s
U_{tip} = tip velocity, m/s
U^* = friction velocity, m/s
X_3 = axial distance, mm
ϵ = rate of dissipation of turbulent kinetic energy, m^2/s^3
Λ = integral scale
ν = kinematic viscosity (m^2/s)

Literature Cited

Abbot, I. H., and A. E. von Doenhoff, *Theory of Wing Sections*, Dover, New York (1959).

Bugay, S., *Analyse Locale des Échelles Caractéristiques du Mélange: Application de la Technique P.I.V. aux Cuves Agitées*, Thèse de Doctorat de l'Institut National des Sciences Appliquées, Toulouse, France (1998).

Bakker, A., K. J. Myers, R. W. Ward, and C. K. Lee, "The Laminar and Turbulent Flow Pattern of a Pitched Blade Turbine," *Trans. Inst. Chem. Eng.*, **74**(A), 485 (1996).

Chapple, D., and S. M. Kresta, "The Effect of Geometry on the Stability of Flow Patterns in Stirred Tanks," *Chem. Eng. Sci.*, **49**(21), 3651 (1994).

Cutter, L. A., "Flow and Turbulence in a Stirred Tank," *AIChE J.*, **12**, 35 (1966).

Derksen, J. J., and H. E. A. van den Akker, "Large Eddy Simulations on the Flow Driven by a Rushton Turbine," *AIChE J.*, **45**, 209 (1999).

Derksen, J. J., M. S. Doelman, and H. E. A. van den Akker, "Three-Dimensional LDA Measurements in the Impeller Region of a Turbulently Stirred Tank," *Exp. Fluids*, **27**, 522 (1999).

Ducoste, J. J., M. C. Clark, and R. J. Weetman, "Turbulence in Flocculators: Effects of Tank Size and Impeller Type," *AIChE J.*, **43**, 328 (1997).

Eggels, J. G. M., F. Unger, M. H. Weiss, J. Westerweel, R. J. Adrian, R. Friedrich, and F. I. M. Nieuwstadt, "Fully Developed Turbulent Pipe Flow: A Comparison Between Direct Numerical Simulation and Experiment," *J. Fluid Mech.*, **268**, 175 (1994).

Escudié, R., *Hydrodynamique et Turbulence par P.I.V. dans Une Cuve Agitée*, Diplome d'Etude Approfondie (D.E.A.), Institut National des Sciences Appliquées, Toulouse, France (1998).

Escudié, R., A. Liné, and P. Kiener, "Analysis of Pseudo-Periodic and Turbulent Fluctuations Induced by a So-Called Axial Impeller at High and Low Reynolds Number," (2002).

Escudié, R., A. Liné, and M. Roustan, "Turbulent Macroscale in the Impeller Stream of a Rushton Turbine," *Eur. Conf. on Mixing*, Delft, The Netherlands, p. 353 (2000).

Essemiani, K., *Analyse Locale des Cuves Agitées Mécaniquement: Potentialités de la Mécaniiue des Fluides Numériques*, Thèse de Doctorat de l'Université Paul Sabatier, Toulouse, France (2000).

Laufer, J., "The Structure of Turbulence in Fully Developed Pipe Flow," *NACA Rep.*, 1174 (1954).

Lee, K. C., and M. Yiannekis, "Turbulence Properties of the Impeller Stream of a Rushton Turbine," *AIChE J.*, **44**(1), 13 (1998).

Mahouast, M., G. Cognet, and R. David, "Two-Component LDV Measurements in a Stirred tank," *AIChE J.*, **35**(11), 1770 (1989).

Mavros, P., P. Xuereb, and J. Bertrand, "Determination of 3-D Flow Fields in Agitated Vessels by Laser-Doppler Velocimetry: Effect of Impeller Type and Liquid Viscosity on Liquid Flow Patterns," *Trans. Inst. Chem. Eng.*, **74**(A), 658 (1996).

Michelet, S., "Turbulence et Dissipation au Sein d'un Réacteur Agité par Une Turbine Rushton—Vélocimétrie Laser Doppler à Deux Volumes de Mesure," Thèse de doctorat de l'Institut National Polytechnique de Lorraine, Nancy, France (1998).

Myers, K. J., R. W. Ward, and A. Bakker, "A Digital Particle Image Velocimetry Investigation of Flow Field Instabilities of Axial Flow Impellers," *J. Fluids Eng.*, **119**, 623 (1997).

Naude, I., C. Xuereb, and J. Bertrand, "Direct Prediction of the Flows Induced by a Propeller in an Agitated Vessel Using an Unstructured Mesh," *Can. J. Chem. Eng.*, **73**, 631 (1998).

Perrard, M., N. Le Sauze, C. Xuereb, and J. Bertrand, "Characterisation of the Turbulence in a Stirred Tank Using P.I.V.," *Proc. Eur. Conf. on Mixing*, Delft, The Netherlands, p. 345 (2000).

Van der Molen, K., and H. R. E. van Maanen, "Laser-Doppler Measurements of the Turbulent Flow in Stirred Vessels to Establish Scaling Rules," *Chem. Eng. Sci.*, **33**, 1161 (1978).

Van't Riet, K., W. Bruijn, and J. M. Smith, "Real and Pseudo-Turbulence in the Discharge Stream from a Rushton Turbine," *Chem. Eng. Sci.*, **31**, 407 (1976).

Van't Riet, K., and J. M. Smith, "The Trailing Vortex System Produced by Rushton Turbine Agitators," *Chem. Eng. Sci.*, **30**, 1093 (1975).

Weetman, R. J., and J. Y. Oldshue, "Power Flow and Shear Flow Characteristics of Mixing Impellers," *Proc. Eur. Conf. on Mixing*, Pavia, p. 43 (1988).

Wu, H., and G. K. Patterson, "Laser-Doppler Measurements of Turbulent Flow Parameters in a Stirred Mixer," *Chem. Eng. Sci.*, **44**, 2207 (1989).

Zhou, G., and S. M. Kresta, "Impact of Tank Geometry on the Maximum Turbulence Energy Dissipation Rate for Impellers," *AIChE J.*, **42**, 2476 (1996a).

Zhou, G., and S. M. Kresta, "Distribution of Energy Between Convective and Turbulent Flow for Three Frequently Used Impellers," *Trans. Inst. Chem. Eng.*, **74**(A), 379 (1996b).

Manuscript received Mar. 14, 2001, and revision received Aug. 3, 2001.